Journal of Contaminant Hydrology 205 (2017) 12–24

Contents lists available at ScienceDirect

Journal of Contaminant Hydrology

journal homepage: www.elsevier.com/locate/jconhyd

Monitoring the evolution and migration of a methane gas plume in an unconfined sandy aquifer using time-lapse GPR and ERT

Colby M. Steelman[a,*], Dylan R. Klazinga[b], Aaron G. Cahill[a,1], Anthony L. Endres[b], Beth L. Parker[a]

[a] G^{360} Institute for Groundwater Research, College of Engineering and Physical Sciences, University of Guelph, 50 Stone Road East, Guelph, ON N1G 2W1, Canada
[b] Department of Earth and Environmental Sciences, University of Waterloo, 200 University Ave West, Waterloo, ON N2L 3G1, Canada

ARTICLE INFO

Keywords:
Stray gas
Fugitive methane
GPR
ERT
Groundwater contamination
Borden aquifer

ABSTRACT

Fugitive methane (CH_4) leakage associated with conventional and unconventional petroleum development (e.g., shale gas) may pose significant risks to shallow groundwater. While the potential threat of stray (CH_4) gas in aquifers has been acknowledged, few studies have examined the nature of its migration and fate in a shallow groundwater flow system. This study examines the geophysical responses observed from surface during a 72 day field-scale simulated CH_4 leak in an unconfined sandy aquifer at Canadian Forces Base Borden, Canada, to better understand the transient behaviour of fugitive CH_4 gas in the subsurface. Time-lapse ground-penetrating radar (GPR) and electrical resistivity tomography (ERT) were used to monitor the distribution and migration of the gas-phase and assess any impacts to groundwater hydrochemistry. Geophysical measurements captured the transient formation of a CH_4 gas plume emanating from the injector, which was accompanied by an increase in total dissolved gas pressure (P_{TDG}). Subsequent reductions in P_{TDG} were accompanied by reduced bulk resistivity around the injector along with an increase in the GPR reflectivity along horizontal bedding reflectors farther downgradient. Repeat temporal GPR reflection profiling identified three events with major peaks in reflectivity, interpreted to represent episodic lateral CH_4 gas release events into the aquifer. Here, a gradual increase in P_{TDG} near the injector caused a sudden lateral breakthrough of gas in the direction of groundwater flow, causing free-phase CH_4 to migrate much farther than anticipated based on groundwater advection. CH_4 accumulated along subtle permeability boundaries demarcated by grain-scale bedding within the aquifer characteristic of numerous Borden-aquifer multi-phase flow experiments. Diminishing reflectivity over a period of days to weeks suggests buoyancy-driven migration to the vadose zone and/or CH_4 dissolution into groundwater. Lateral and vertical CH_4 migration was primarily governed by subtle, yet measurable heterogeneity and anisotropy in the aquifer.

1. Introduction

Methane gas (CH_4) leakage associated with conventional and unconventional oil and gas activities, particularly abandoned legacy wells and most recently shale gas development, poses a risk to freshwater aquifers (Kelly et al., 1985; Osborn et al., 2011; Jackson et al., 2013). As a result, robust monitoring strategies are needed to assess gas leakage pathways from the well bore (Dusseault et al., 2000), impacts to regional water quality (Vidic et al., 2013), and to understand broader implications to the environment and society as a whole (The Royal Society, 2012; Council of Canadian Academies, 2014). Safe and responsible development of conventional and unconventional (i.e., shale or tight rock) natural gas resources hinges on the advancement of suitable conceptual models of fugitive CH_4 migration in the subsurface, based on multiple lines of evidence acquired across a range of spatial and temporal scales (Cahill et al., 2017).

Although the risk of stray CH_4 leakage into aquifers during oil and gas development has been consistently recognized as a potential threat or concern to the environment, few studies have provided insight into the nature of its migration, impact on and fate in groundwater. Consequently a field experiment to simulate CH_4 leakage was conducted in a shallow unconfined sandy aquifer at Canadian Forces Base (CFB) Borden, Canada, to assess impacts of fugitive CH_4 on groundwater, including free-phase mobility and resultant effects on groundwater hydrochemistry. The use of the Borden aquifer was a key component of the experimental design since this aquifer has been the focus of high-resolution hydrologic characterization and field experiments since the late 1970′s (Sudicky and Illman, 2011). This background

---

[*] Corresponding author at: G^{360} Institute for Groundwater Research, College of Engineering and Physical Sciences, University of Guelph, 50 Stone Rd East, Guelph, ON N1G 2W1, Canada.

E-mail address: csteelma@uoguelph.ca (C.M. Steelman).

[1] Department of Earth, Ocean and Atmospheric Sciences, University of British Columbia, 2329 West Mall, Vancouver, BC V6T 1Z4, Canada.

http://dx.doi.org/10.1016/j.jconhyd.2017.08.011
Received 9 February 2017; Received in revised form 15 August 2017; Accepted 27 August 2017
Available online 30 August 2017

permitted comparison of our results to previous studies in the same aquifer where observations were under natural conditions, including actual geologic heterogeneity and groundwater flow dynamics.

The propensity for non-aqueous phase liquids to spread laterally when encountering interfaces of contrasting permeability has been observed during numerous dense non-aqueous phase liquid (DNAPL) release experiments within the Borden aquifer, based on direct or indirect observations of immiscible fluid migration before, during and after the injection phase (e.g., Brewster and Annan, 1994; Brewster et al., 1995; Thomson, 2004; Hwang et al., 2008). Analogous behaviours of immiscible-phase fluids have been observed through buoyancy-driven vertical gas migration during an air-sparging experiment within the same Borden aquifer (Tomlinson et al., 2003). All of these studies noted that subtle variations in permeability led to extensive lateral migration of the immiscible-phase liquid parallel to bedding. Roy et al. (2016) explored mechanisms influencing free- and dissolved-phase CH_4 migration and fate within an unconfined sandy aquifer loosely based on the Borden aquifer by numerically simulating a well-bore leakage event. However, prior to this study no one had performed a controlled CH_4 leakage experiment in a shallow naturally bedded aquifer to assess migration and fate of CH_4 originating from a pressurized release point, analogous to casing vent flow or well-bore leakage rates typically observed in the conventional and unconventional oil and gas industry (Dusseault et al., 2000).

This paper aims to show, for the first time under controlled conditions, the dynamic characteristics of free CH_4 gas migration and its 3D distribution in the subsurface emanating from point sources under pressure to better understand hydrogeologic controls on the spatio-temporal evolution of a gas-phase plume in an unconfined aquifer. Ground-penetrating radar (GPR) and electrical resistivity tomography (ERT) were used to capture the 2D and 3D geometry of the gas distribution at selected times and evaluate the role of natural sedimentological structures and hydrogeologic conditions in a non-destructive manner. These indirect geophysical observations, specifically tailored to monitoring the gas-phase component, represents a constituent of a multi-disciplinary experiment to examine the movement, impacts, and fate of free- and dissolved-CH_4 injected into the shallow freshwater aquifer (Cahill et al., 2017).

Our geophysical observations demonstrate how subtle variations in silt and fine sand laminations within the largely medium-grained sandy aquifer can guide free-phase gas parallel to bedding in the direction of groundwater flow. We observed a strong influence of anisotropy and evidence of dynamic multi-phase fluid saturations and mobility causing transient (episodic) lateral migration events within the aquifer. Based on these observations we conclude that substantial lateral mobility of CH_4 can occur at much farther distances and within shorter timeframes than those based on groundwater flow velocities, before commencement of attenuation through dissolution or upward migration and exsolution into the vadose zone.

2. Background

2.1. Multi-phase flow in porous media

Gas flow through a saturated pore space will depend on a combination of geologic and fluid properties. Parameters such as pore geometry and wettability determine capillary pressures, which in turn, will affect fugitive gas migration and behaviour over time. Meanwhile, the viscosity and density of the groundwater and gas, as well as buoyancy forces, solubility, gaseous diffusion coefficients, Henry's Law and aspects of the fugitive gas source including leakage rates, pressures, and gradients will contribute to multi-phase flow. For a comprehensive review of these processes and their interaction the reader is referred to Wardlaw (1982). Although these micro-to-meso-to-macroscopic characteristics may be visible due to mineral contrasts in laminations, they can be difficult to measure (Sellwood et al., 2005), and thus, may limit the predictive capacity of field-scale numerical models (Thomson and Johnson, 2000).

Plampin et al.'s (2014) study examined pertinent principles of multi-phase flow in water-saturated porous media (Lenormand et al., 1988) by injecting CO_2-saturated water through an extensive set of experiments performed in a column packed with layers of sand with varying grain-size. The authors quantitatively explained how different geologic facies with varying distances between interfaces (i.e., vertical heterogeneity) can have vastly different effects on gas-phase migration. Most notably, they found that interfaces with less-permeable sediment over more-permeable sediment will affect gas saturations more often and more significantly than interfaces with the opposite layering configuration; this so-called enhancement of gas evolution as a result of heterogeneity could be predicted through an analysis of dissolved gas saturation, distance between vertical heterogeneities and the leakage location, and fundamental properties of the porous media. While their laboratory experiment focused on buoyancy-driven (i.e., vertical) CO_2 migration in a horizontally layered system, it provided insights into gas accumulation and temporal behaviours at permeability transitions at field-scale.

Previous studies have recognized the importance of subsurface heterogeneities in gas-phase migration, distribution, and fate in groundwater systems (e.g., Gurevich et al., 1993; Thomson and Johnson, 2000; Duncan, 2013); however, few have directly examined the natural conditions governing gas migration. The vast majority of experimental gas injections into a saturated fresh water aquifer have focused on CO_2 (e.g., Lamert et al., 2012; Trautz et al., 2012; Cahill et al., 2014; Yang et al., 2014) or air (e.g., Lundegard and LaBrecque, 1995; McKay and Acomb, 1996; Tomlinson et al., 2003). The solubility of CO_2 in water is relatively high, which combined with its propensity for reactive transport makes its behaviour very different than that of air; yet, the principles of multi-phase flow will be the same for both gases. Much like air, the solubility of CH_4 in water is relatively low, and thus it should exhibit an analogous behaviour.

Roy et al. (2016) numerically simulated CH_4 behaviour from a leaky decommissioned hydrocarbon well in a typical unconfined sandy aquifer, loosely based on Borden aquifer parameters. Based on their multi-phase flow and reactive transport simulations, free-phase gas will rapidly migrate upward along the production well (i.e., well-bore), progressively dissolving in groundwater along its path. Assuming a homogenous and isotropic system, this vertical migration along the well-bore will initiate once the CH_4 solubility is reached. In this case, limited lateral migration of CH_4 gas would occur, with aerobic CH_4 oxidation limiting the dissolved CH_4 concentration 5 m downgradient. However, previous chlorinated solvent DNAPL migration experiments in the Borden aquifer above and below the water table (e.g., Poulsen and Kueper, 1992; Kueper et al., 1993; Brewster et al., 1995; Broholm et al., 1999; Thomson, 2004) and air-injection experiments for solvent removal (e.g., Tomlinson et al., 2003) have shown that multi-phase flow and non-wetting phase saturations will be strongly affected by subtle variations in grain-size layering. Consequently, the gas-phase component will have a propensity to migrate horizontally in the aquifer within relatively coarser-grained sand layers (Tomlinson et al., 2003), and eventually, vertically due to buoyant forces. Thus, it is expected that the lateral extent of free-gas in the Borden aquifer will be dependent on the contrast in vertical hydraulic conductivity between adjacent finite-length layers and their lateral connectivity within a bedded sand facies.

2.2. Geophysical monitoring of multi-phase fluids

Near-surface geophysical methods can be powerful tools to non-invasively characterize micro-to-macroscopic processes by exploiting the electrical properties of water, rock and the immiscible fluid (Slater, 2007; Knight et al., 2010; Binley et al., 2015). While much of the early geophysical studies were focused on non-aqueous phase liquids in porous saturated sediment, these works led to significant contributions to the conceptual understanding of multi-phase flow dynamics (e.g., Brewster and Annan, 1994; Brewster et al., 1995; Daily and Ramirez, 1995; Hwang et al., 2008). Geophysics has been used to explore the complex behaviour of free-phase gas migration in saturated environments through numerous remediation air-sparging experiments (e.g., Schima et al., 1996; McKay and Acomb, 1996; Tomlinson et al., 2003).

Recent concerns regarding long-term impacts of CH_4 and CO_2 fluxes to atmosphere – through carbon storage technologies or climate change scenarios – has led to novel geophysical applications aimed at monitoring and understanding the mechanisms controlling free-phase gas migration in the subsurface. Geophysical responses associated with gas migration and associated geochemical processes on the aqueous environment have been examined within biogenic CH_4 emitting peatlands (e.g., Slater et al., 2007; Comas et al., 2008; Strack and Mierau, 2010; Parsekian et al., 2011; Terry et al., 2016), geothermal gas vents (e.g., Pettinelli et al., 2008), and through simulated CO_2 injection experiments (e.g., Auken et al., 2014; Doetsch et al., 2015; Yang et al., 2015; Lassen et al., 2015). All of these studies have explored the various mechanisms and subsurface conditions influencing or governing free-phase gas dynamics in heterogeneous environments.

For instance, Terry et al. (2016) used time-lapse electrical resistivity to assess mechanisms governing free-phase biogenic CH_4 (e.g., ebullition and buoyancy-driven migration) in a peatland environment. The authors noted transient decreases in free-phase CH_4 beneath a low-permeable barrier, which they attributed to the formation of a rupture in the confining layer. They concluded that ebullition events and free-phase CH_4 transfer were largely controlled by changes in atmospheric pressure and subsurface structures. While their work highlights the capacity of high-resolution electrical methods in the characterization of complex and episodic gas release events in shallow groundwater environments, the nature of a non-point or variably distributed CH_4 source in a peatland is expected to be different than that of a point source arising from a leaky petroleum well in a lithostratigraphic environment.

3. Methodology

3.1. Field site and experimental setup

The simulated CH_4 leakage experiment was conducted at Canadian Forces Base (CFB) Borden, Ontario, Canada, within the sand pit study area characterized by a shallow unconfined aquifer with a water table approximately 1 ± 0.5 m below ground surface (bgs) depending on the season (Sudicky and Illman, 2011). The injection site is located 300 m downgradient from an old landfill with a broadly distributed contaminant plume (MacFarlane et al., 1983) that persists in the lowermost portion of the aquifer beneath the study site. Locally, the aquifer extends 7–9 m bgs and is underlain by a thick clayey silt aquitard. The aquifer is generally described as a homogeneous, clean, well-sorted medium to fine-grained Pleistocene beach sand. Our test site is located approximately 80 m east of the Tomlinson et al. (2003) air-sparging experiment and within 10 m of the Bunn et al. (2011) pumping test study.

CH_4 was injected into the aquifer over a 72 day period (injection initiated on July 15, 2015) through a pair of vertically-aligned sparging wells plunging at 45° from horizontal and orthogonal to the groundwater flow direction (Fig. 1). Gas was injected in the aquifer using two electronic mass flow controllers connected to polyethylene tubing with sparging screens positioned at 4.5 and 9.0 m bgs (Fig. 2). In total, 51.35 m^3 of CH_4 was injected into the aquifer at rates ranging from 0.17 to 4.6 m^3/day (Table 1); these rates represent the low to medium range in surface casing vent flows observed in Alberta and British Columbia, Canada (Nowamooz et al., 2015). It is worth noting that the rates considered in this study are considerably lower than the air-injection rate used by Tomlinson et al. (2003) (e.g., 200 m^3/day over 7 days from a single point 3 m below the water table), and much lower than CH_4 leakage scenarios deemed critical by regulatory agencies (i.e., > 300 m^3/day) (Nowamooz et al., 2015).

Thirty-two bundle-tube samplers were installed for multi-level groundwater monitoring. They were constructed of 6 mm polyethylene tubing with a 5 cm long geotextile covered screen (Fig. 2), primarily arranged in a regular grid with increased areal distances between locations along the direction of groundwater flow (Fig. 1b). The complete groundwater monitoring network consisted of 112 depth-discrete sampling points; however, only a subset of the data collected from these samplers are presented in this paper (identified in Fig. 2). All subsurface installations were completed using a Geoprobe™ direct push rig using a knock-out disposable bit (i.e., no core was retrieved). Due to the high water table (1 m bgs) and sandy aquifer material, the annuli readily collapsed around the tubing once the drill rods were removed. A more detailed description of the injection design and field setup can be found in Cahill et al. (2017).

A number of surface-based and downhole gas monitoring instruments were installed around the immediate injection area. While these data sets are not discussed in this paper, the permanent placement of these sensors did impede GPR data acquisition or influence the radar signal nearest the injection site. Specifically, three metal LI-COR chambers (LI-8100-104) were positioned directly above, 1.5 m behind, and 2 m east the injection point (Fig. 1b). These chambers were connected to a power supply located within the CH_4 tank storage area. Sampling tubes and power cords that connected these sensors to the trailer were bundled together and laid on the ground surface along the central axis of the study plot. Continuous total dissolved gas sensors were installed within two subsurface access tubes located 1.5 and 5 m downgradient from the injection. These sensors were accompanied by a battery and multiplexer housed in a fiberglass box placed at ground surface as shown in Fig. 1b.

3.2. Groundwater and soil sampling

A suite of hydrochemical samples were collected across the groundwater monitoring network before, during and after the injection periods (Fig. 3). This study uses elements of the total dissolved gas pressure (P_{TDG}) (accuracy: ± 1 mmHg) and specific electrical conductance (EC) data collected using a multi-parameter water quality sonde and flow-through cell (Manta 2, Eureka Water Probes, Austin, Texas) with a peristaltic pump at a low flow rate (40–50 ml/min); measurements were obtained at ground surface and represent steady-state conditions during sample pumping (monitored points around the injectors are identified in Fig. 1b and Fig. 2). Although the P_{TDG} measurements will be subject to in-well degassing and ebullition (Manning et al., 2003), impacts on individual samples are assumed constant over the study period given the consistent sampling methodology. Here, the act of pumping the water through the flow-through cell at surface will effectively lead to an underestimate in the true P_{TDG} due to lower pressure (Roy and Ryan, 2010). Henry's law states that the partial pressure exerted by a dissolved gas phase will be proportional to its concentration in solution. Thus, as methane is injected into the aquifer, measured changes in the relative magnitude of P_{TDG} can provide an indirect indication of gas-phase dynamics (i.e., pressure buildups in response to gas accumulation in the aquifer and pressure releases as accumulated or temporary entrapped gas migrates beyond a capillary barrier).

A continuous soil core was collected post-injection using a Geoprobe™ to a depth of 9 m bgs near the injection point (refer to Fig. 1b). Soil permeability was measured using a falling-head permeameter with repacked samples of 5 cm length (Fig. 4). The core was logged for general lithology characteristics (e.g., bedding orientation, mineralogy and lamination thicknesses) with representative samples of visually distinct units extracted for grain-size distributions (Fig. 4).

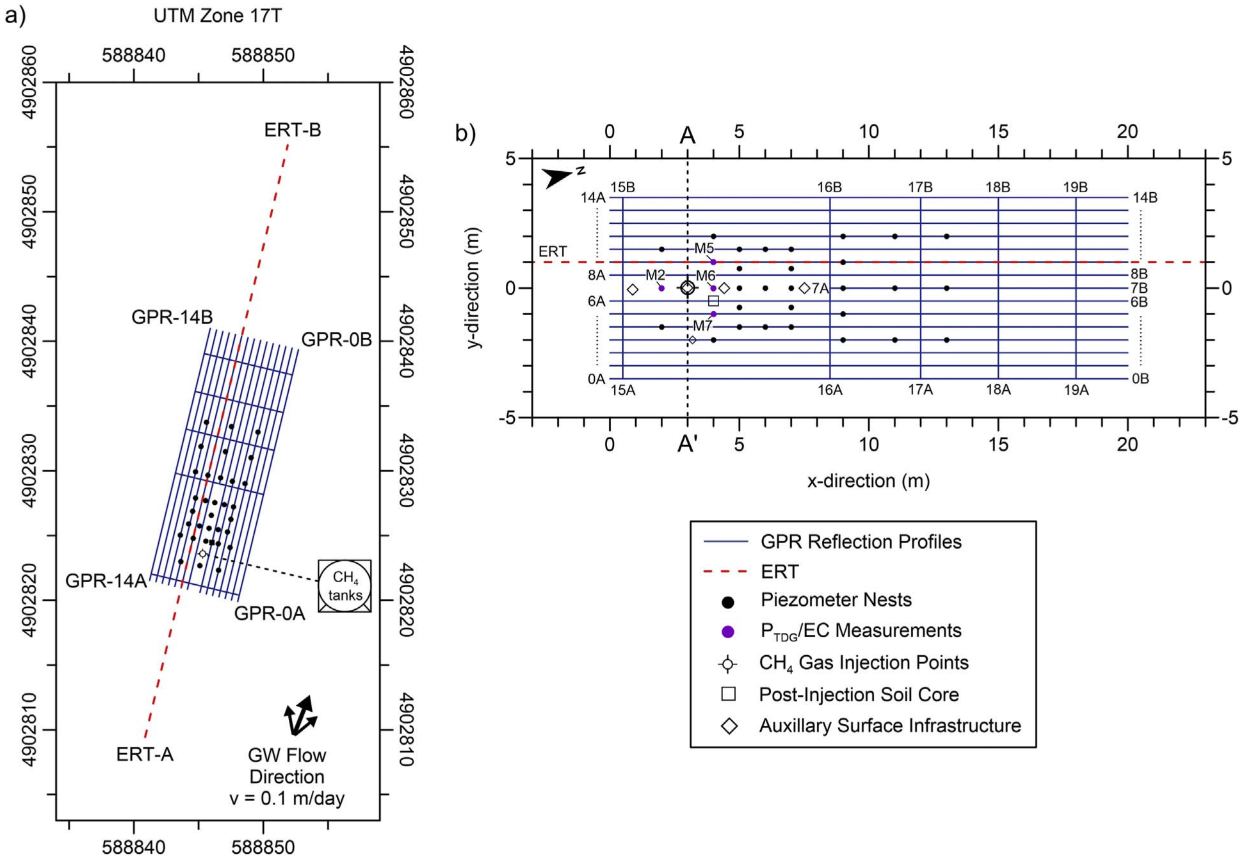

Fig. 1. (a) Site map of ground-penetrating radar (GPR), electrical resistivity tomography (ERT) and hydrochemistry monitoring network around CH_4 injection points. (b) GPR (Lines 0–14) and ERT profiles were collected parallel to groundwater flow direction with GPR tie-lines (Lines 15–19) collected orthogonal to flow; line orientations are denoted as A (start) and B (end).

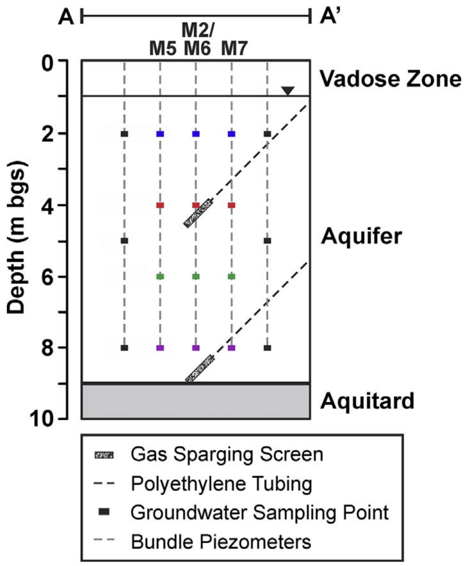

Fig. 2. Cross-section of the injection plane showing nearby groundwater monitoring network 1.0 m offset to CH_4 injection points along vertical section A-A′ (Fig. 1b). Bundle piezometers considered in this study include M2, M5, M6 and M7 (refer to Fig. 1b), which provide depth-discrete groundwater samples at 2 m (blue), 4 m (red), 6 m (green) and 8 m (purple) below ground surface. (For interpretation of the references to colour in this figure legend, the reader is referred to the web version of this article.)

Table 1
Summary of CH_4 injection rates at 1.013 bar and 15 °C. A total of 34.9 kg of CH_4 was released into the subsurface over a 72 day period.

Phase	Elapsed time	Duration	Injection rates		Cumulative volume[a]
			Shallow	Deep	
	(days)		(L/min)		(m)
I	28	28	0.06	0.06	4.68
II	68	40	0.35	0.35	41.15[b]
III	70	2	0.00	0.35	42.17
IV	72	2	1.50	1.50	51.35
V	128	56	–	–	–

[a] Based on mass flow controller readout.
[b] Injection stopped during power outage from day 39 (14:30) to 43 (19:30).

3.3. Time-lapse ERT profiling

An electrical resistivity tomography (ERT) profile was collected along the long-axis of the GPR grid (refer to Fig. 1a). The ERT line was offset 1 m to the west relative to the CH_4 injection points to avoid the auxiliary infrastructure and cabling located along the central axis of the study plot (note the shorter coverage of Line 7A/B in Fig. 1b due to the auxiliary surface infrastructure and cabling). ERT data were acquired using a Syscal Switch Jr. (Iris Instruments, Orleans, France) connected to 48 electrodes spaced 1 m apart. The same sequence of dipole-dipole arrays with 402 measurement points was used for each acquisition event. ERT data were collected immediately after the completion of the GPR measurements, with snapshots collected on a daily to weekly interval (refer to Fig. 3). Two resistivity equipment malfunctions occurred during Phase I of the injection which resulted in missed ERT sampling

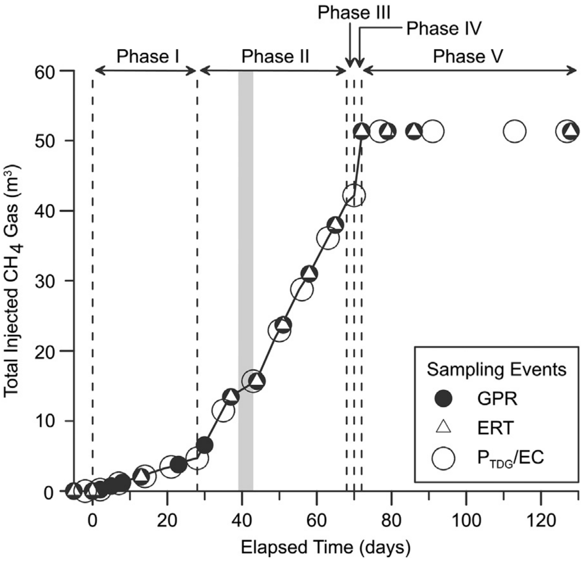

Fig. 3. Cumulative CH_4 injected into aquifer with ground-penetrating radar (GPR), electrical resistivity tomography (ERT), total dissolved gas pressure (P_{TDG}), and specific electrical conductance (EC) sampling events. Two background geophysical (day − 5 and 0) and one hydrochemical (day − 2) sampling events occurred prior to commencement of the injection at the end of day 0. Grey shaded region denotes 4 day power outage (Table 1).

events on days 2, 5, 8, 23 and 30.

Apparent resistivity data were filtered to remove erroneous data points prior to being inverted using RES2DINV v.3.59 (Geotomo Software, Malaysia), which uses the Gauss-Newton smoothness-constrained least-squares method (Loke and Dahlin, 2002). A sequential time-lapse inversion was performed with a robust smoothness constraint and low initial damping factors optimized at each inversion; model refinement was used to reduce the impact of large resistivity contrasts along the surface. The initial background model represents an average between two pre-injection surveys completed on days − 5 and 0. These two datasets exhibited a median apparent resistivity difference of 2% across 402 readings. Inverse model root mean squared (RMS) errors for the subsequent time-lapse inversions were low (< 2%) indicating good convergence between the modelled and measured datasets.

3.4. Time-lapse GPR reflection profiling

GPR data were collected using a PulseEKKO 100 GPR system (Sensors & Software, Mississauga, Canada) equipped with 200 MHz bistatic (unshielded) antennas and 1000 V transmitter. GPR reflection data were acquired along a series of parallel 20 m lines spaced 0.5 m apart connected by five orthogonal tie-lines (Fig. 1b). Traces were recorded using a spatial step-size of 0.1 m with the antennas spaced 0.5 m apart and orientated perpendicular to the survey line direction. A 64 trace stack was used with a temporal sampling interval of 800 ps over a 300 ns time-window. Data were recorded using a manual trigger and measuring tapes before, during, and after the active injection phases (refer to Fig. 3).

Post-acquisition GPR data processing and visualization were performed using ReflexW (v.7) (Sandmeier Software, Germany). The basic processing work-flow consisted of: a high-pass mean dewow filter to remove dc shifts on individual traces; zero-time corrections; a spreading and exponential gain function to compensate for attenuation; a band-pass frequency filter (25–75–250–325 MHz); a notch frequency filter (40–85–85–125 MHz) to suppress surface metal effects and electrical interferences (ringing) on selected trace ranges near the auxiliary sensors and cabling; and a 3-trace horizontal filter for lateral smoothing. It should be noted that signal processing used to remove auxiliary sensor artifacts from the GPR profiles likely diminished signals associated with free-gas migration near the injector. Finally, a complex trace analysis (i.e., instantaneous amplitude) was used to assess changes in reflectivity strength. The instantaneous amplitude was calculated across the entire GPR area for each sampling event using an inverse distance weighting method across a uniformly discretized 0.25 (x, y, z) grid.

The depth axis was generated using a fixed radar velocity of 0.06 m/ns; this value is consistent with previous GPR studies in the Borden sand pit (e.g., Tomlinson et al., 2003; Hwang et al., 2008) and velocities observed from common-midpoint (CMP) soundings collected during the experiment. During the injection, CMPs were collected at the midpoint of each of the orthogonal tie lines (Lines 15–19; Fig. 1b) at each

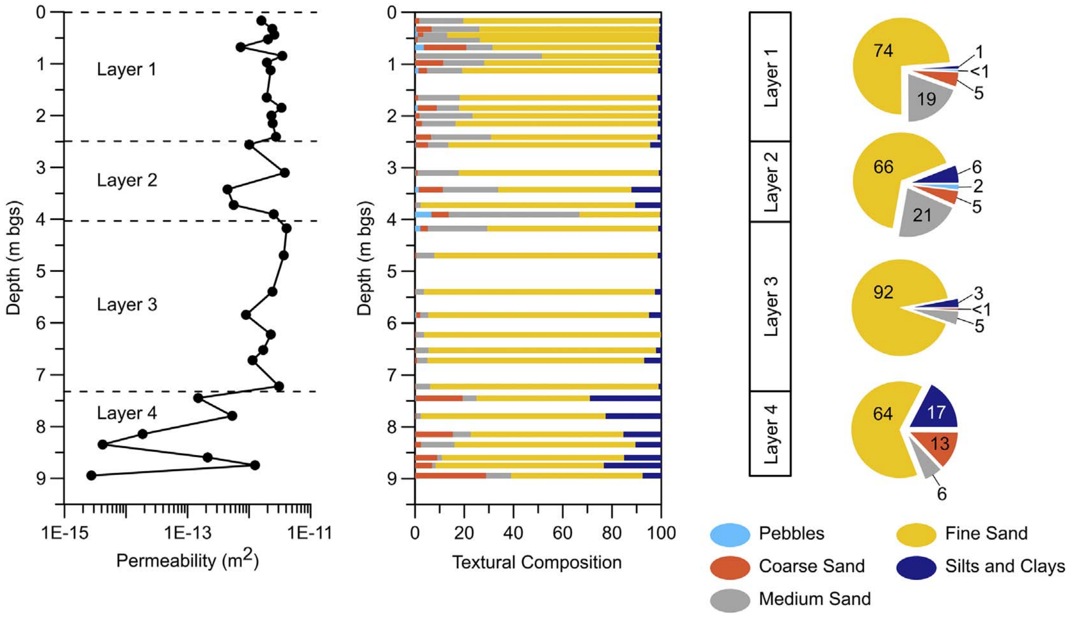

Fig. 4. Falling-head permeameter derived permeability profile from 5 cm samples selected from continuous soil core near the injection point with corresponding grain-size distributions. Generalized layer model based on sedimentological characteristics (bedding frequency and grain-size distribution). Layers 2 and 4 represents relatively lower permeable layers based on higher percentages of silts and clay. CH_4 was injected at the top of Layer 3 and bottom of Layer 4.

sampling event. However, the complex and transient behaviour of gas-phase migration and distribution in the subsurface (i.e., variable dielectric permittivity), elevated noise around the injection area, combined with the absence of strong and continuous dielectric boundaries across the site, hindered our ability to identify reliable and spatially consistent vertical velocity profiles over the full duration of the experiment. Therefore, we limit our interpretation of the GPR measurements to changes in reflection amplitude observed within the areas characterized by discontinuous stratigraphic bedding. Site conditions limited GPR signal penetration to approximately 5 m below the water table, thereby limiting our ability to track changes in reflectivity at the deep injection horizon. Minor adjustments to the position of auxiliary infrastructure (e.g., LI-COR chambers and cabling) occurred during the injection which may have introduced some signal artifacts around the immediate injection area; this includes the removal of all auxiliary sensors prior to final measurement round.

4. Results

4.1. Aquifer heterogeneity

The continuous core collected near the injection location revealed vertical variability in permeability throughout the vertical profile (3.5 orders of magnitude range; Fig. 4) determined from re-packed permeameters; corresponding grain-size analyses on the samples indicate these variations are associated with increased percentages of silt and clay within fine sand layers (Fig. 4). Soil samples were collected from visually distinct units; thus, higher sample frequency would imply more textural variability (i.e., grain-scale bedding). The permeability and grain-size data were classified into 4 main groups based on their general grain-size distributions and bedding frequency: Layers 1 and 3 represent relatively more permeable zones with higher percentages of fine sand with little or no silt and clay, while Layers 2 and 4 correspond to less-permeable layers with lower percentage of fine sand and higher percentages of silt and clay. Layer 4 captures the transition into the underlying clayey-silt aquitard. The core revealed a thin layer (from 3.9–4.2 m bgs) of clean, medium to coarse-grained sand with pebbles underlying Layer 2. Layers 1 and 4 exhibited more internal laminations creating vertical heterogeneity (i.e., stronger or higher permeability contrasts) than Layers 2 and 3, the latter of which exhibited an upward reduction in textural variability.

4.2. Porewater response to methane injection

Average P_{TDG} (Fig. 5a) and aqueous specific electrical conductance (EC) (Fig. 5b) are shown for each depth interval based on bundle tube piezometers M2, M5, M6 and M7 (Figs. 1b and 2) located near the injection site for the full duration of the experiment. While similar P_{TDG} and EC measurements were collected at other locations across the monitoring network, the fact that they were selectively sampled resulted in partial or variable data coverage over the monitoring period.

Episodic fluctuations in P_{TDG} (Fig. 5a) were observed during the injection period (− 4% to + 5% of the mean value for the study duration at a given depth) with the highest pressures and greatest fluctuations occurring at 4 m and 6 m depths. Two major peaks in P_{TDG} were observed during the injection phase: one around day 14 in the middle of Phase I, and a second around days 50/56 during the middle to latter half of Phase II. This was followed by a sudden decrease on day 63 and increase on day 70 at the end of Phase III. P_{TDG} generally converged and stabilized after the injection ceased on day 72 through day 128. Based on these data, the timing of the pressure peaks do not appear to be linked to changes in the injection rate (Table 1).

Corresponding EC measurements (Fig. 5b) appears to show less erratic fluctuations over the injection period (− 15% to + 24% of the mean value for the study duration at a given depth) with the greatest fluctuations occurring at 4 m and 6 m depths. EC measurements within the old landfill plume are captured at the 8 m sampling depth; data from depths 2, 4 and 6 m, above the old plume, exhibit values an order of magnitude lower but remain within a factor of 1 or 2 of each other. The EC data exhibits slight periodicity and time-lag relative to the changes in P_{TDG}, with modest and somewhat gradual peaks arising around days 21 (end of Phase I) and 70 (end of Phase II) at all four sample depths. While the EC responses appear to be episodic, with the largest increase occurring in the latter half of Phase II between days 56–70, the peaks were very subtle. Nevertheless, a systematic increase in EC was observed at 2, 4 and 6 m depths during the injection phase, followed by a moderate decrease and return to pre-injection conditions through day 128.

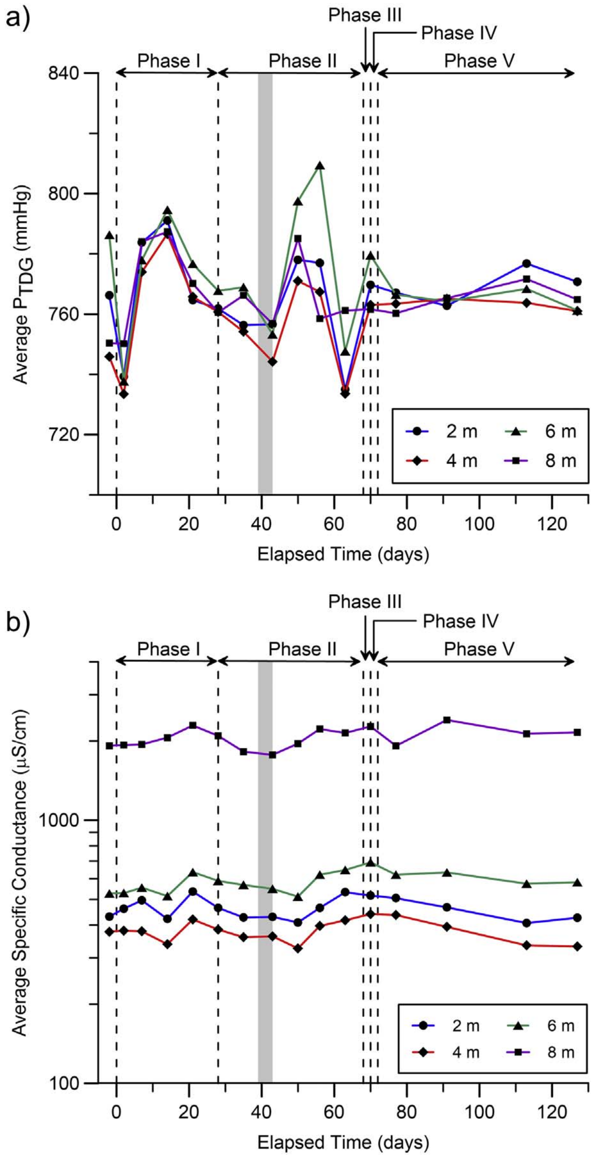

Fig. 5. (a) Average total dissolved gas pressure (P_{TDG}) and (b) porewater specific electrical conductance (EC) obtained during hydrochemical sampling events near the injection plane (i.e., M2, M5, M6, M7 in Fig. 1b) at levels 2, 4, 6 and 8 m bgs. Note: hydrochemical sampling dates do not exactly coincide with GPR/ERT sampling dates (refer to Fig. 3). Grey region represents power outage.

4.3. Time-lapse ERT monitoring

Time-lapse ERT models (Fig. 6) captures changes in the resistivity of the aquifer immediately downgradient from the shallow injector. The background model (day 0), which is based on the average of two

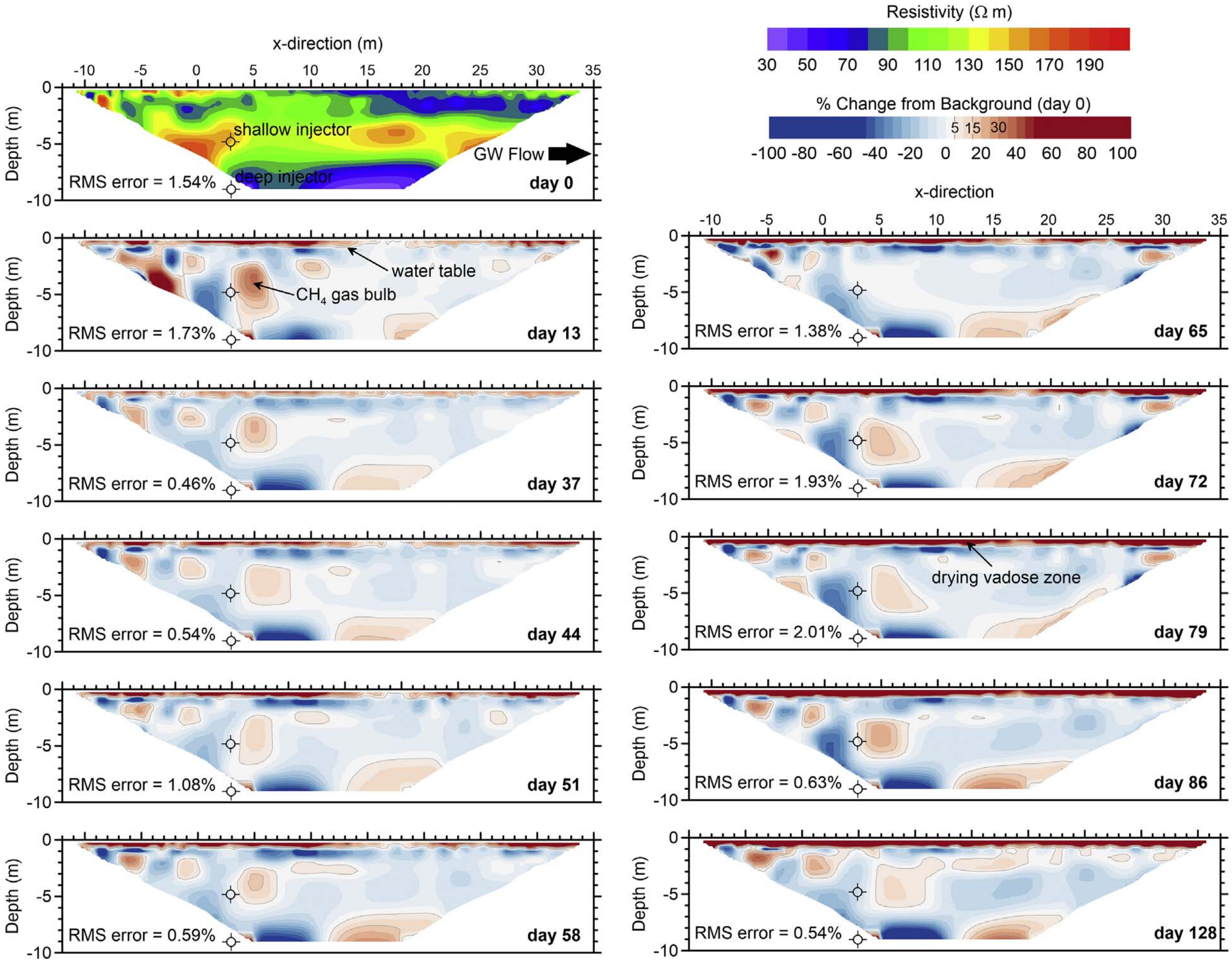

Fig. 6. Time-lapse ERT models showing changes in electrical resistivity distribution relative to average background conditions (days − 5 and 0). Inverted background resistivity profile (day 0) shows the transition into the old landfill plume at approximately 7 m bgs. The shallow injection is located within the uncontaminated portion of the aquifer while the deep injection point is located within the landfill plume. Root mean squared (RMS) error is provided for each model result; values (< 2%) indicate good model convergence with low noise. A systematic increase in resistivity was observed between 0 and 1 m bgs as the experiment progressed, which is consistent with a lowering water table and drying vadose zone. Initial conditions are consistent with a seasonally high water table (~ 0.5 m bgs) and predominantly wet soil conditions. The gas bulb observed downgradient the shallow injector is defined by a resistivity increase > 5% relative to background.

apparent resistivity data sets collected 5 and 0 days before the injection commenced, reveals a three layer system: a low resistivity zone at depths > 6.5 m corresponding to the old landfill plume and clay aquitard; an intermediate zone of high resistivity between 2.5 and 6.5 m depth showing lateral discontinuities in resistivity structure; and an upper zone of moderate to low resistivity that encompasses the transition into the vadose zone between 0.5 and 1.5 m bgs.

Measurements on day 13 of the injection show both increases and decreases in the resistivity around the shallow injector. Here, a marked resistivity increase of > 30% occurred on the downgradient side of the shallow injector from 3 to 8 m position (x-direction) between 2 and 6 m bgs in the form of a resistivity bulb. Here, the lateral extent or boundary of the gas bulb near the injector was defined by a resistivity increase > 5% relative to background. Measurements on day 37 show that the bulb had reduced in size and resistivity. From day 37–58, the bulb began to increase in size, with a lobe emanating from the main bulb, spreading downgradient below a depth of 2 m (i.e., top of intermediate zone of high resistivity) with resistivity fluctuations varying between 5% and > 15%. By day 65, resistivity conditions around the shallow injector and within the intermediate zone approached background conditions, thus suggesting a reduction in CH_4 gas saturation. However, by day 72 the high resistive zone or bulb had re-established around the shallow injector, with resistivities once again fluctuating between 5% and > 15% above background. Surveys completed post-injection show a persistent high resistivity zone downgradient from the shallow injector, reaching a maximum relative change on day 86, 14 days after the injection was turned off. Resistivity slowly diminished around the injector while progressively increasing farther downgradient within the top of the intermediate zone by day 128.

During this experiment groundwater temperatures measured from pressure transducers located within monitoring wells outside the experimental test plot remained reasonably constant, ranging from 8 to 9 °C. Empirical evidence has shown that resistivity can decrease anywhere from 1% to 2.5% per °C (Campbell et al., 1948; Keller, 1989; Brassington, 1998). Therefore, natural temperature fluctuations in the aquifer would have had a negligible impact on the observed ERT dynamics. A large increase in resistivity was observed within the upper meter of vadose zone particularly after day 44. This increase is likely associated with a reduction in soil moisture due to higher evapotranspiration and more limited precipitation combined with a seasonal reduction in water table elevation.

4.4. *Time-lapse GPR reflectivity monitoring*

Fig. 7 presents the results of a single GPR reflection profile collected along Line 9, coincident with a portion of the ERT profile (refer to Fig. 1b) and roughly represents the centreline of the lateral gas migration pathway. This surface GPR reflection profile captured a

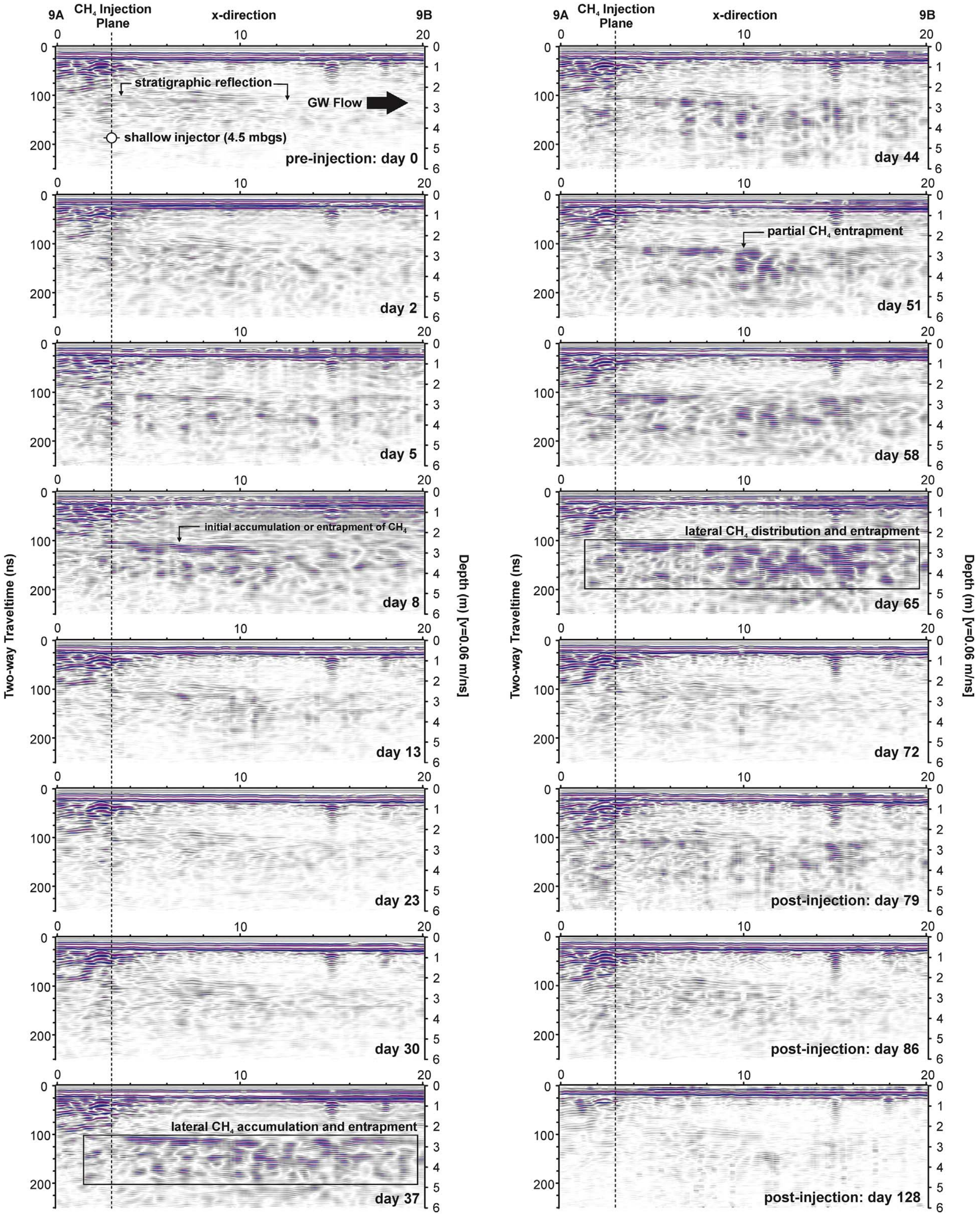

Fig. 7. Time-lapse GPR reflection profiles collected along Line 9A/B (1 m offset from the CH_4 injection points) directly overlying the ERT profile. Increased reflectivity occurred within a package of continuous reflectors located between 2.5 and 4.5 m bgs. Injection period was accompanied by episodic fluctuations in amplitude with peak reflectivity occurring on days 8, 37 and 65.

dynamic geophysical response to gas-phase CH_4 in the aquifer. The majority of the reflectivity changes occurred between 100 and 200 ns corresponding to a zone comprised of variably connected stratigraphic bedding 2.0–4.5 m bgs (i.e., Layer 2 in Fig. 4). A progressive increase in the reflection amplitude along and below a relatively continuous reflector at 100 ns was observed from day 0 to 8, after which reflectivity decreased, reaching a relative low on day 23. A slight increase in reflectivity was observed on day 30 (Phase I injection rate), followed by a more substantial increase across the full profile on day 37 (9 days after Phase II initiated). Reflectivity dropped on day 44 (coincident with a 4 day power outage), and exhibited slight variations through day 58. By day 65 reflection amplitudes reached their maximum observed values

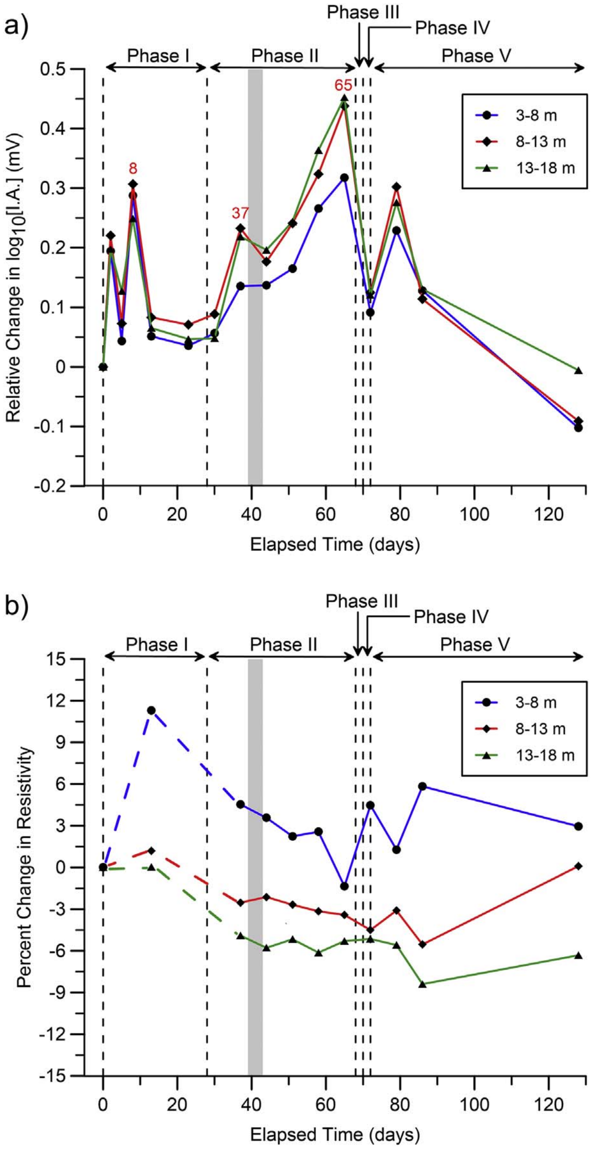

Fig. 8. a) Relative changes in GPR $\log_{10}$(instantaneous amplitude) and b) percentage change in ERT model resistivity from 1.5 to 6.0 m bgs; dashed lines for ERT denotes missed measurements due to an equipment malfunction. Datasets correspond to 3–8 m, 8–13 m, and 13–18 m intervals along ground surface along the co-located ERT and GPR Line 9A/B. These data show some oscillation and spatial variability over the active injection period. Peak GPR amplitude fluctuations (days 8, 37, and 65) appear more dynamic and transient than the corresponding resistivity measurements. Grey region represents power outage.

for the experiment; the bulk of the response was constrained been 2.5–4.5 m bgs (100–200 ns). The survey completed on day 72, just before the injection ceased, showed a drop in reflectivity over the full profile. Yet, subsequent post-injection measurements showed a slight increase in reflectivity on day 79 (7 days after the injection ceased), followed by a gradual return to background conditions from days 86 to 128. Reflectivity variations were episodic with peak reflectivity observed on days 8, 37 and 65; the relative timing of these events indicates that they are not likely associated with increases in the injection rate (Table 1). Furthermore, these GPR amplitude variations largely occurred within the region defined by continuous stratigraphic reflection events (below a depth of 2 m). Based on the core log, this zone is defined by more frequent variations in permeability and soil texture. Modest fluctuations in reflectivity were observed above a depth of 2 m which would indicate buoyant (upward) migration of gas toward the vadose zone.

4.5. Spatiotemporal trends in geophysical and porewater response

Fig. 8 presents the relative change in GPR instantaneous amplitude (along line 9A/B) and percentage change in model resistivity from 3 to 18 m (x-direction; Fig. 1b) between 1.5 and 6.0 m bgs; relative variations in amplitude and percentage change in model resistivity were broken-down into intervals 3–8 m, 8–13 m and 13–18 m along ground surface downgradient from the injection point. Episodic fluctuations in GPR amplitude (Fig. 8a) were more transient in the first half of Phase I, exhibiting a consistent response across each of the three intervals. A slightly larger initial response was observed closer to the injection (i.e., 3–8 m and 8–13 m) with slightly higher amplitudes observed between 8 and 13 m, before stabilizing across the site through the latter half of Phase I. Amplitudes progressively increased through Phase II, with 8–13 m and 13–18 m intervals exhibiting a consistently higher response relative to the 3–8 m interval. Measurements collected at the end of Phase IV (prior to the end of the injection) show a strong and systematic reduction in amplitude across each interval, generally converging toward pre-injection conditions. After the injection ceased (Phase V) a spike in amplitude was observed on day 79 within each interval, with slightly higher responses between 8 and 13 m and 13–18 m; this period was followed by a return to background conditions on day 86. The final set of measurements was collected on day 128, with all auxiliary surface infrastructure removed; this resulted in a slightly negative response for the zones closest to the injection location relative to background.

While the ERT profiles (Fig. 6) revealed the formation of a high resistivity bulb and lobe extending downgradient from the shallow injector, the bulk response within each of the three intervals (Fig. 8b) was more subtle compared to the GPR. Nevertheless, conditions within the 3–8 m interval did show a marked increase in resistivity during Phase I, before gradually declining through Phase II; this response is consistent with the initial formation of the resistivity bulb (Fig. 6) observed downgradient from the shallow injector. Conversely, the 8–13 m and 13–18 m intervals both showed a gradual, yet systematic decrease in resistivity relative to background through the entire active injection period; this decrease in resistivity is consistent with the increase in EC observed near the injectors between 2 and 6 m depths. Transient fluctuations in resistivity were again observed near the injector between the end of Phase II and Phase IV, after which, resistivities showed convergence toward background conditions across each interval.

The overall sensitivities of the ERT and GPR measurements to changes in electrical properties within the aquifer were quite different (Figs. 5, 6 and 7); the most notable differences being the GPR's higher sensitivity to gas accumulation along stratigraphic boundaries further away from the resistivity bulb, and the absence of reflectivity changes near the shallow injector where the resistivity showed the largest changes. Furthermore, the integrated resistivity response within the three spatial (x-distance) intervals (Fig. 8b) appeared to be less-sensitive to short-period transients captured by the GPR (Fig. 8a); fewer ERT measurement events perhaps missed some of the early-time Phase I perturbations. The Pearson product-moment correlation coefficient (r) between the GPR and ERT datasets in Fig. 8 were calculated as follows: 3–8 m ($r = -0.53$, $N = 9$, $p = 0.007$), 13–18 m ($r = -0.44$, $N = 9$, $p = 0.002$), and 13–18 m ($r = -0.17$, $N = 9$, $p < 0.001$). These results indicate a moderate to weakly negative correlation between the two measurements (i.e., an increase in amplitude was accompanied by a reduction in resistivity), which suggests these measurements may be sensitive to different attributes or physical characteristics of the evolving free-phase CH_4 plume.

A comparison between GPR trends (Fig. 8a) and P_{TDG} trends near the injection plane (Fig. 5a) reveals that sharp reductions in P_{TDG} were accompanied by an increase in reflectivity (e.g., days 42 and 62). Similarly, periods of elevated P_{TDG} corresponded to lower GPR amplitude (e.g., days 15 and 50). This inverse relationship was particularly evident between day 51 and 72 (i.e., last 3 measurements in Phase II through to the end of Phase IV). Here, P_{TDG} reached a local maximum on day 50/56, after which, P_{TDG} rapidly decreased reaching a low on day 63 before rebounding thereafter. The EC of the porewater around the injection plane (Fig. 5b) exhibited subtle, yet mutually consistent fluctuations through the active injection period. However, relative to the P_{TDG}, measured transients in EC was less abrupt, and generally exhibited longer-period fluctuations. The overall trend in EC at 2, 4 and 6 m increased over the injection, which is consistent with the systematic decrease in resistivity observed further downgradient between 1.5 and 6 m bgs. Relatively sharp increases in EC near the end of Phase I and II also seem to correspond to short-period declines in formation resistivity; however, large fluctuations observed in the resistivity near the injector between 3 and 8 m (Fig. 8b; day 13 and day 79) were not readily evident in the EC time-series. It is important to note that the geophysical measurements were not collected on the same dates as the P_{TDG} and EC measurements (refer to Fig. 3), which may explain some of these ambiguities. Furthermore, P_{TDG} and EC represent conditions at 4 points (M2, M5, M6 and M7) surrounding the injectors, while the geophysics represents the cumulative response between three intervals along a 2D plane parallel to groundwater flow (GPR Line 9A/B).

4.6. Spatiotemporal extent of episodic methane gas-phase plume

GPR reflectivity reached temporal maximums on day 8, 37 and 65. The instantaneous amplitude was calculated over the study plot using the full reflection profile data set (Lines 0A/B through 19A/B; Fig. 1). Fig. 9 provides the change in the instantaneous amplitude distribution relative to background conditions on day 0 for these three local maximum periods. Representative depth slices were extracted across the data cubes at 1.5, 3, 4.5 and 6 m bgs based on a uniform velocity of 0.06 m/ns. These energy distributions show variations in the spatial extent (vertical and horizontal) and magnitude of the radar amplitude induced by the injected CH_4 gas in the upper half of the aquifer.

Early-time conditions on day 8 display a broadly impacted zone, with predominant changes observed horizontally in the positive y-direction (west) downgradient from the shallow injector; the magnitude of this response decreased with depth. Conditions midway through the injection on day 37 indicate a reduction in amplitudes near the water table (i.e., 1.5 m bgs) accompanied by an increase farther down the section between 4.5 and 6 m bgs. These changes remained downgradient from the injection plane, with the bulk response occurring within the northwestern quadrant of the GPR grid. The highest reflectivity response occurred on day 65; here, reflectivity continued to increase around 4.5 m bgs, while increasing slightly near the water table compared to day 37. Amplitudes also increased farther into the northeastern quadrant of the GPR grid.

Fig. 10 shows spatiotemporal changes in radar amplitude for the period between days 51–72 encompassing the largest lateral and volumetric extent of free-gas in the aquifer on day 65. Here, the isosurface encompasses a zone with changes in $\log_{10}$(instantaneous amplitude) > 0.429; this value corresponds to the maximum observed difference between the two background GPR surveys (day − 5 and 0), and thus represents a conservative estimate of the maximum noise level or natural variability in the system. Based on the ERT profiles in Fig. 6, the ongoing injection of CH_4 appears to have led to the formation of a gas bulb adjacent the shallow injector. The formation of a gas bulb was accompanied by a systematic increase in P_{TDG} pressure (Fig. 5a). According to the time-lapse ERT data, this bulb remained relatively stable in size and shape until the gas exceeded the entry pressure of the less-permeable material immediately downgradient the shallow injector (note the lateral discontinuity in the background resistivity within the intermediate zone in the background model in Fig. 6). Based on the observed drop in P_{TDG} on day 63 (Fig. 5a), together with the disappearance of the resistive bulb on day 65 (Fig. 6), and emergence of elevated reflectivities on day 65 (Fig. 7), this period is thought to represent a major CH_4 migration event where a pressurized gas release led to the substantial lateral migration of free-gas into the adjacent aquifer. Here, CH_4 gas extended to distances > 17 m downgradient in the direction of groundwater flow, during which, only moderate changes in reflectivity (i.e., gas entrapment) were observed around the shallow injection well and upgradient of the injection plane. Based on the transient nature of the GPR response (Fig. 10), free-phase CH_4 preferentially-migrated downgradient, spreading laterally within a zone of fine to medium-grained sand with limited silt beneath a lower-permeable layer at 3.5 m bgs (Fig. 4), occurring at least three times during the active injection experiment (Fig. 9).

5. Discussion and conclusions

The ERT and GPR responses associated with the presence and migration of CH_4 gas in the aquifer, together with P_{TDG} and EC measurements collected near the injector, provided complementary information about its spatiotemporal behaviour during the field experiment simulating a CH_4 leakage event. Localized resistivity increases identified in the inverted models (3–8 m downgradient), particularly on day 8, together with the relatively limited changes observed in EC, suggest that the bulk of the resistivity response was associated with significant localized reductions in porewater saturation. The resistivity changes observed farther downgradient (8–13 and 13–18 m

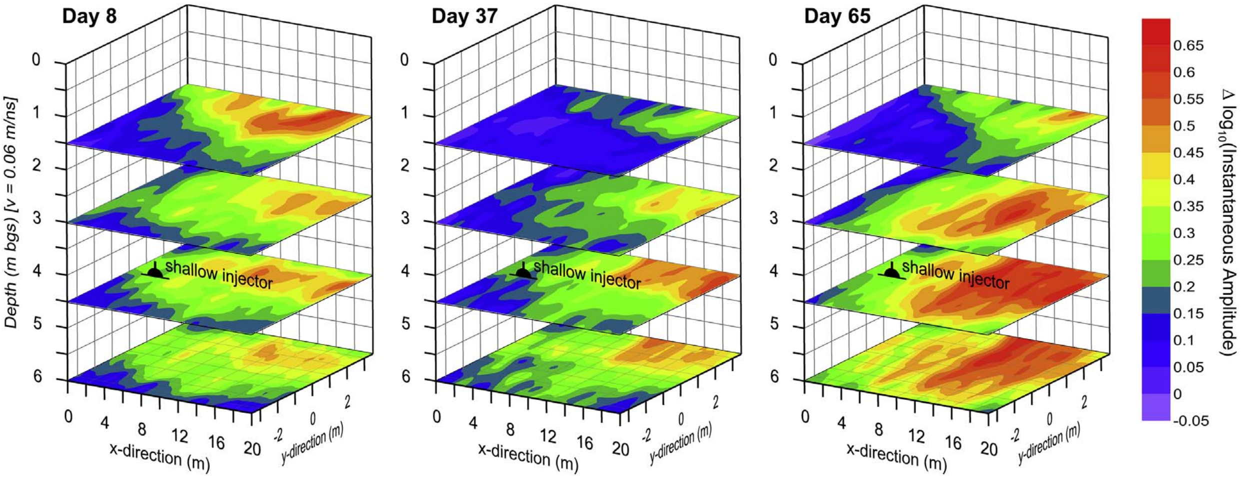

Fig. 9. Extracted amplitude-depth slices from the change in instantaneous amplitude cube based on 3D inverse distance gridding of the full GPR dataset (refer to Fig. 1b). Datasets capture peak amplitude on day 8, 37 and 65. Peak amplitude changes were highest near the water table (approximately 1 m bgs) at early time (day 8), while later times (day 37 and 65) show stronger response at and below the shallow (4.5 m) injection well with relatively reduced response near the water table.

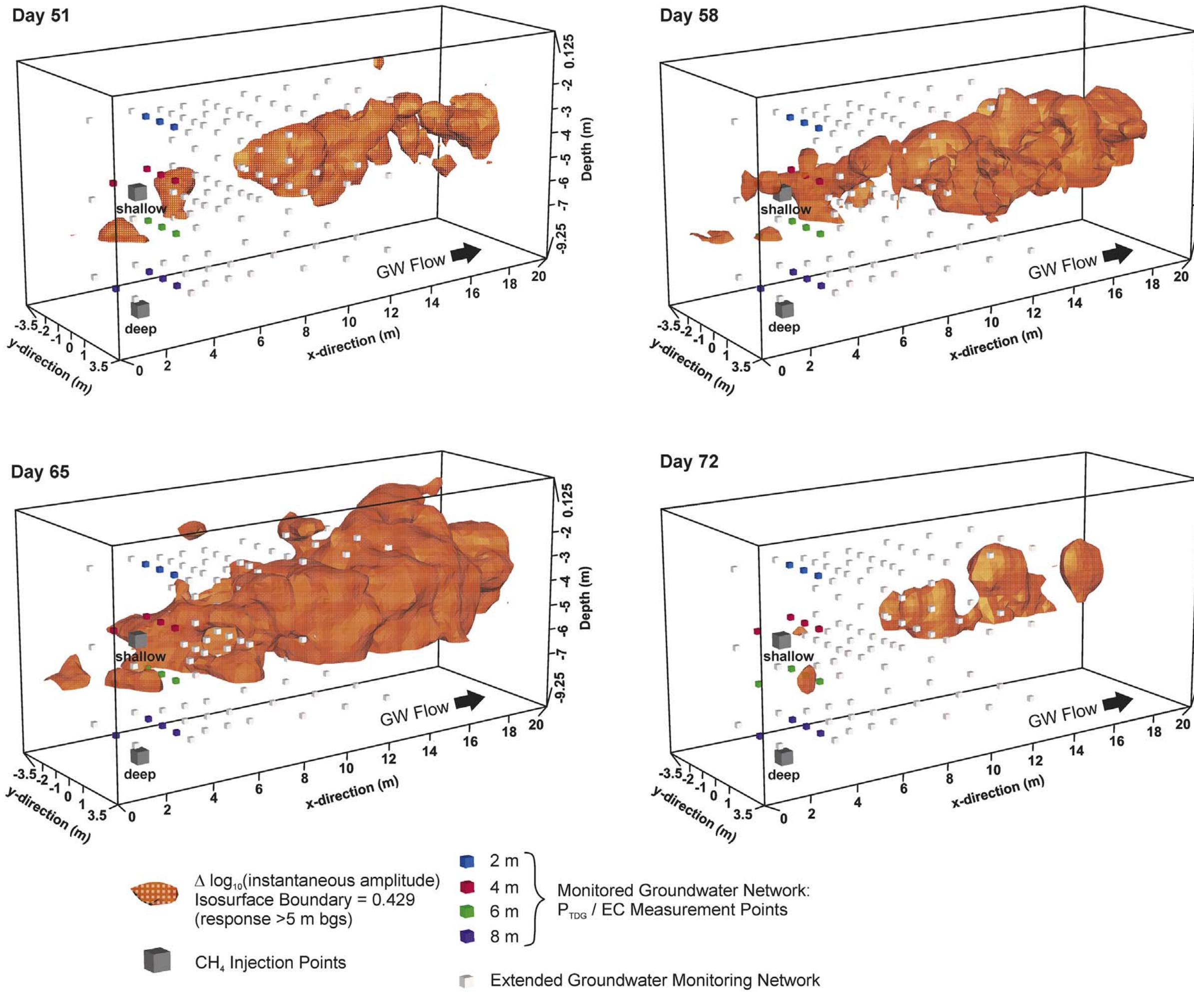

Fig. 10. Relative change in $\log_{10}$(instantaneous amplitude) over the study area before and after an episodic migration event on day 65. GPR amplitudes > 0.429 are enclosed within the isosurface boundary that is equal to the maximum observed background fluctuation. CH_4 injection points and P_{TDG}/EC measurement locations (identified in Fig. 5) are shown here within the extended groundwater monitoring network. The period between days 51 to 72 captured a major CH_4 release event into the aquifer. A period of high P_{TDG} (days 50 and 56 in Fig. 5a) was accompanied by reduced reflectivity (day 51 and 58 in Fig. 7). A sudden drop in P_{TDG} (day 63 in Fig. 5a) was followed by an increase in reflectivity along the sand layers (day 65 in Fig. 7). Afterwards, P_{TDG} rebounded slightly (day 70 in Fig. 5a) along with reduced reflectivity (day 72 in Fig. 7).

from the injectors) do not indicate significant desaturation of the porespace by CH_4 gas, thereby suggesting limited sensitivity to lateral gas spreading and entrapment beneath subtle permeability contrasts. Based on these observations, ERT was most sensitive to the region around the shallow injector, and did capture the formation of an isolated gas bulb and laterally extending lobe downgradient.

GPR was most sensitive to changes in the dielectric contrast along coherent reflection events (i.e., pre-existing bedding boundaries) similar to that concluded by Tomlinson et al. (2003) for air migration, and also observed by Brewster et al. (1995); Hwang et al. (2008) and Thomson (2004) with chlorinated solvent DNAPL migration and distributions, all in the Borden aquifer. Gradual desaturation of porewater below low-permeable layers led to a reduction in dielectric permittivity; the strongest GPR responses were observed further downgradient when CH_4 pressures around the injectors exceeded the entry pressure of the adjacent materials, thereby permitting lateral migration of free-phase gas and subsequent entrapment beneath subtle grain-scale bedding. GPR was not successful in imaging the formation of the gas bulb near the injector, possibly due to the presence of a gradational change in saturation around the lateral extent of the bulb, absence of resolvable sedimentary boundaries, or due to auxiliary infrastructure signal interference. Nevertheless, GPR indicates that the CH_4 preferentially migrated downgradient under pressure, where it could spread and disperse across the aquifer more readily. These GPR observations are consistent with those made in Tomlinson et al. (2003)'s air-sparging experiment, in terms of preferential direction and lateral extent of gas-phase migration from the injection point, i.e., initially, most (but not all) of the gas migrates laterally along higher permeability beds creating a well-behaved plume emanating from the injection points; after which, the upward migration of gas due to buoyancy slows the lateral extent and eventually effluxes to the vadose zone or dissolves into groundwater.

Based on the GPR response and available permeability data, CH_4 appears to have been guided laterally outward within layers of coarser sand underlying a layer of less-permeable sediment at 3.5 m bgs. A thin layer of medium to coarse-grained sand with pebbles identified in the core from 3.9–4.2 m bgs may have acted as the primary lateral pathway away from the injector; after which, the gas continued in the horizontal direction, facilitated by small-scale geologic layering of varying permeability. Here, the thin, finer, silty sand layers sufficiently impeded upward migration of free-gas, thereby enabling the gas to preferentially migrate laterally between coarser, more permeable sand layers. These sedimentary packages are known to be discontinuous on the order of one to several meters (Sudicky, 1986; Thomson, 2004), which may explain the episodic release(s) and complex spatial-temporal distribution of gas within the aquifer.

Previous studies conducted within the Borden aquifer (e.g., Kueper et al., 1993; Brewster et al., 1995; Broholm et al., 1999) examined the behaviour of a migrating non-aqueous phase liquid (NAPL) in the Borden site unconfined aquifer. Here, preferential accumulation of NAPL was observed within and along thin (mm to cm scaled) layers of coarser grained, well-sorted sand, with minimal or no accumulation of NAPL within the adjacent finer-grained sand laminations. These experiments showed how an infiltrating chlorinated organic solvent NAPL would accumulate and spread along a depositional boundary, with horizontal and dipping coarser laminations acting as preferential pathways resulting in numerous millimeter-thin layers of NAPL; these liquids would persist within these thin layers for extended periods of time relative to the dissolved phase resulting in highly dispersed dissolved-phase plumes. Based on cm-scale vertical sampling of continuous cores, Thomson (2004) showed that these thin sand laminations could be distinguished in terms of permeability with the largest contrasts observed at the boundary between distinct grain-size laminations; these subtle heterogeneities led to spatially complex distributions of NAPL and dissolved-phase plumes in the Borden aquifer (Laukonen et al., 2000). Therefore, preferential accumulation of CH_4 gas and subsequent lateral migration in the aquifer most likely occurred along packages of horizontally stratified, thinly laminated coarser grained sand layers. While these small-scaled laminated features are well below the resolving capacity of the GPR frequency used in this study, the observed geophysical response during the injection is consistent with a zone of layered/interbedded sands.

Roy et al.'s (2016) numerical simulations of CH_4 migration, distribution and fate from a leaky production well within an unconfined aquifer – loosely based on the Borden aquifer – suggested that gas (injected at a constant rate of 2 m^3/day) would primarily flow vertically along the well bore until it reached the water table, contrary to our observations. Based on our geophysical observations and the findings of numerous NAPL experiments at Borden, subtle changes in soil texture (i.e., permeability) such as fine sand layering or slight increases in silt within the aquifer results in observable anisotropy parallel to bedding that will lead to significant lateral migration of free-gas, thus, impacting a much larger zone of groundwater than previously speculated or based on groundwater advection. Therefore, even slight anisotropy in an aquifer, typical of sedimentary systems, will result in more complex free- and dissolved-phase CH_4 plumes than that predicted by uncalibrated multi-phase multi-component and reactive transport models.

Geophysical observations of biogenic CH_4 emissions in peatlands by Terry et al. (2016) proposed that episodic release events may be governed by changes in atmospheric pressure, precipitation events and changes in vadose zone saturation, all playing an important role in the magnitude and timing of CH_4 efflux events. While free-gas migration events were episodic in this study, the somewhat variable correlations and/or timing of perturbations between geophysical and geochemical measurements within the aquifer suggest that several processes are likely influencing gas-phase saturations (e.g., atmospheric pressure, precipitation, vadose zone water content and water table fluctuations) that may not be predictable solely based on the injection rate history and fundamental properties of the porous media; the relative importance of these dynamic processes on evolution of the free- and dissolved-phase methane plumes, as well as the importance of physical and geochemical attributes (e.g., permeability, capillarity, solubility, and gaseous diffusion) of the aquifer will be examined in future work (Cahill et al., 2017).

The geophysical attributes of GPR and ERT showed how the formation of a CH_4 gas bulb through low to moderate leakage rates, can be laterally and vertically constrained by local-scale heterogeneities, yet result in numerous episodic breakout events with extensive, preferential lateral migration into the aquifer. While the CH_4 injection rates considered in this study were substantially lower, and extended over a longer period of time compared to the earlier air-sparging experiment by Tomlinson et al. (2003) in the same aquifer, free-phase CH_4 managed to extend similarly, if not greater distances from the injection site. Once distributed across the aquifer, CH_4 most likely migrated upward to the atmosphere by buoyancy and/or dissolved into groundwater creating a broad and dispersed groundwater plume, which will be the subject of future work.

The following main conclusions are drawn from the geophysical results of this experiment:

1. GPR and ERT identified episodic lateral migration of CH_4 gas within the upper 5 m stemming from gas buildups adjacent the shallow injector, with free-gas mobilized under pressure > 17 m down-gradient;
2. GPR identified significant increases in the reflectivity along subtle sedimentary boundaries indicating an increase in the dielectric contrast at the reflecting interface, which is consistent with CH_4 accumulation and lateral migration along horizontal bedding with slight variability in grain-size distributions or composition;
3. Numerous episodic CH_4 migration events were observed during periods of constant injection rate, which is consistent with systematic buildups in gas saturation necessary to exceed entry pressures of overlying lower permeable sediment, enhancing mobility and dissipation of CH_4 across the aquifer;
4. Observed CH_4 gas plume at the bulk scale was laterally extensive in the direction of groundwater flow, with the majority of the gas preferentially migrating along higher permeability beds; subsequent upward migration of gas due to buoyancy slowed the lateral extent, after which, CH_4 entered the vadose zone or dissolved into groundwater;
5. Strong heterogeneity and anisotropy due to grain-scale bedding in the aquifer enhanced mobility of free-gas resulting in a much larger zone of influence on groundwater than previously speculated or calculated based on groundwater advection.

Although this study considered geophysical responses from surface, both GPR and ERT can be applied in boreholes, which make them suited for monitoring CH_4 leakages into deeper freshwater aquifers. Therefore, surface and borehole geophysical methods would be a well-suited component of any groundwater monitoring program designed to understand the potential impacts associated conventional and unconventional oil and gas activities on overlying freshwater aquifers.

Acknowledgements

This research was made possible through an NSERC Strategic Partnerships Grant Project (SPG-P) awarded to Drs. John Cherry and Beth Parker (principal investigators), and collaborators Drs. Bernhard Mayer, Ulrich Mayer and Cathryn Ryan. Dr. Aaron Cahill provided a major role with proposal writing, experimental design and overall project management, both with field implementation and project reporting, and is now a research associate at the University of British Columbia Department of Earth, Oceanic and Atmospheric Sciences. An NSERC Banting Fellowship provided support to Dr. Colby Steelman.

References

Auken, E., Doetsch, J., Fiandaca, G., Christiansen, A.V., Gazoty, A., Cahill, A.G., Jakobsen, R., 2014. Imaging subsurface migration of dissolved CO_2 in a shallow aquifer using 3-D time-lapse electrical resistivity tomography. J. Appl. Geophys. 101, 31–41. http://dx.doi.org/10.1016/j.jappgeo.2013.11.011.

Binley, A., Hubbard, S.S., Huisman, J.A., Revil, A., Robinson, D.A., Singha, K., Slater, L., 2015. The emergence of hydrogeophysics for improved understanding of subsurface processes over multiple scales. Water Resour. Res. 51. http://dx.doi.org/10.1002/2015WR017016.

Brassington, R., 1998. Field Hydrogeology. John Wiley Sons, Inc.

Brewster, M.L., Annan, A.P., 1994. Ground-penetrating radar monitoring of a controlled DNAPL release: 200 MHz radar. Geophysics 59, 1211–1221.

Brewster, M.L., Annan, A.P., Greenhouse, J.P., Kueper, B.H., Olhoeft, G.R., Redman, J.D., Sander, K.A., 1995. Observed migration of a controlled DNAPL release by geophysical methods. Groundwater 33, 977–987.

Broholm, K., Feenstra, S., Cherry, J.A., 1999. Solvent release into a sandy aquifer. 1. Overview of source distribution and dissolution behavior. Environ. Sci. Technol. 33, 681–690.

Bunn, M.I., Rudolph, D.L., Endres, A.L., Jones, J.P., 2011. Field observation of the response to pumping and recovery in the water table region of an unconfined aquifer. J. Hydrol. 403, 307–320. http://dx.doi.org/10.1016/j.jhydrol.2011.04.011.

Cahill, A.G., Marker, P., Jakobsen, R., 2014. Hydrogeochemical and mineralogical effects of sustained CO2 contamination in a shallow sandy aquifer: A field scale controlled release experiment. Water Resour. Res. 50, 1735–1755. http://dx.doi.org/10.1002/2013WR014294.

Cahill, A.G., Steelman, C.M., Forde, O., Kuloyo, O., Ruff, E., Mayer, B., Mayer, K.U., Strous, M., Ryan, M.C., Cherry, J.A., Parker, B.L., 2017. Mobility and persistence of methane in groundwater in a controlled release field experiment. Nat. Geosci. 10, 289–294. http://dx.doi.org/10.1038/NGEO2919.

Campbell, R.B., Bower, C.A., Richards, L.A., 1948. Change of electrical conductivity with temperature and the relation of osmotic pressure to electrical conductivity and ion concentration for soil extracts. Soil Sci. Soc. Am. Proc. 12, 66–69.

Comas, X., Slater, L., Reeve, A., 2008. Seasonal geophysical monitoring of biogenic gases in a northern peatland: Implications for temporal and spatial variability in free phase gas production rates. J. Geophys. Res. 113, G01012. http://dx.doi.org/10.1029/2007JG000575.

Council of Canadian Academies, 2014. Environmental Impacts of Shale Gas Extraction in Canada. Ottawa (ON): The Expert Panel on Harnessing Science and Technology to Understand the Environmental Impacts of Shale Gas Extraction. Council of Canadian Academies.

Daily, W., Ramirez, A., 1995. Electrical resistance tomography during in-situ trichloroethylene remediation at the Savannah River Site. J. Appl. Geophys. 33, 239–249.

Doetsch, J., Fiandaca, G., Auken, E., Christiansen, A.V., Cahill, A.G., Jakobsen, R., 2015. Field-scale time-domain spectral induced polarization monitoring of geochemical changes induced by injected CO_2 in a shallow aquifer. Geophysics 80, WA113–WA126. http://dx.doi.org/10.1190/GEO2014-0315.1.

Duncan, I., 2013. The bubble/slug flow model for methane leakage from natural gas wells as an analogue for shallow CO_2 migration. Energy Procedia 37, 4692–4697. http://dx.doi.org/10.1016/j.egypro.2013.06.378.

Dusseault, M.B., Gray, M.N., Nawrocki, P.A., 2000. Why Oilwells Leak: Cement Behavior and Long-Term Consequences. In: Proceedings of the SPE International Oil and Gas Exhibition, SPE Paper 64733, Beijing, China.

Gurevich, A.E., Endres, B.L., Robertson Jr., J.O., Chilingar, G.V., 1993. Gas migration from soil and gas fields and associated hazards. J. Pet. Sci. Eng. 9, 223–238.

Hwang, Y.K., Endres, A.L., Piggott, S.D., Parker, B.L., 2008. Long-term ground penetrating radar monitoring of a small volume DNAPL release in a natural groundwater flow field. J. Contam. Hydrol. 97, 1–12. http://dx.doi.org/10.1016/j.jconhyd.2007.11.004.

Jackson, R.B., Vengosh, A., Darrah, T.H., Warner, N.R., Down, A., Poreda, R.J., Osborn, S.G., Zhao, K.G., Karr, J.D., 2013. Increased stray gas abundance in a subset of drinking water wells near Marcellus shale gas extraction. Proc. Natl. Acad. Sci. U. S. A. 110, 11250–11255.

Keller, G.V., 1989. Section V: electrical Properties. In: Carmichael, R.S. (Ed.), CRC Practical Handbook of Physical Properties of Rock and Minerals. CRC Press, pp. 361–427.

Kelly, W.R., Matisoff, G., Fisher, J.B., 1985. The effects of a gas-well blow-out on groundwater chemistry. Environ. Geol. Water Sci. 7, 205–213.

Knight, R., Pyrak-Nolte, L.J., Slater, L., Atekwana, E., Endres, A., Geller, J., Lesmes, D., Nakagawa, S., Revil, A., Sharma, M.M., Straley, C., 2010. Geophysics at the interface: Response of geophysical properties to solid-fluid, fluid-fluid, and solid-solid interfaces. Rev. Geophys. 48, RG4002. http://dx.doi.org/10.1029/2007RG000242.

Kueper, B.H., Redman, D., Starr, R.C., Reitsma, S., Mah, M., 1993. A field experiment to study the behaviour of tetrachloroethylene below the water table: spatial distribution of residual and pooled DNAPL. Groundwater 31, 756–766.

Lamert, H., Geistlinger, H., Werban, U., Schütze, C., Peter, A., Hornbruch, G., Schulz, A., Pohlert, M., Kalia, S., Beyer, M., Großmann, J., Dahmke, A., Dietrich, P., 2012. Feasibility of geoelectrical monitoring and multiphase modeling for process understanding of gaseous CO_2 injection into a shallow aquifer. Environ. Earth Sci. 67, 447–462. http://dx.doi.org/10.1007/s12665-012-1669-0.

Lassen, R.N., Plampin, M., Sakaki, T., Illangasekare, T.H., Gudbjerg, J., Sonnenborg, T.O., Jensen, K.H., 2015. Effects of geologic heterogeneity on migration of gaseous CO_2 using laboratory and modeling investigations. Int. J. Greenh. Gas Control 43, 213–224. http://dx.doi.org/10.1016/j.ijggc.2015.10.015.

Laukonen, K.A., Parker, B.L., Cherry, J.A., 2000. Internal characteristics of a bromide tracer zone during natural flow in the Borden aquifer, Ontario, Canada. Tracers and Modelling in Hydrogeology. In: Proceedings of TraM'2000 Conference. 262. IAHS Publication, Liege, Belgium, pp. 227–233.

Lenormand, R., Touboul, E., Zarcone, C., 1988. Numerical models and experiments on immiscible displacement in porous media. J. Fluid Mech. 189, 165–187.

Loke, M.H., Dahlin, T., 2002. A comparison of the Gauss-Newton and quasi-Newton methods in resistivity imaging inversion. J. Appl. Geophys. 49, 149–162.

Lundegard, P.D., LaBrecque, D., 1995. Air sparging in a sandy aquifer (Florence, Oregon, U.S.A.): actual and apparent radius of influence. J. Contam. Hydrol. 19, 1–27.

MacFarlane, D.S., Cherry, J.A., Gillham, R.W., Sudicky, E.A., 1983. Migration of contaminants in groundwater at a landfill – a case study. 1. Groundwater flow and plume delineation. J. Hydrol. 63, 1–29.

Manning, A.H., Solomon, D.K., Sheldon, A.L., 2003. Applications of a total dissolved gas pressure probe in ground water studies. Groundwater 41, 440–448.

McKay, D.J., Acomb, L.J., 1996. Neutron moisture probe measurements of fluid displacement during in situ air sparging. Ground Water Monit. Remediat. 16, 86–94.

Nowamooz, A., Lemieux, J.-M., Molson, J., Therrien, R., 2015. Numerical investigation of methane and formation fluid leakage along the casing of a decommissioned shale gas well. Water Resour. Res. 51, 4592–4622. http://dx.doi.org/10.1002/2014WR016146.

Osborn, S.G., Vengosh, A., Warner, N.R., Jackson, R.B., 2011. Methane contamination of drinking water accompanying gas-well drilling and hydraulic fracturing. Proc. Natl. Acad. Sci. U. S. A. 108, 8172–8176.

Parsekian, A.D., Comas, X., Slater, L., Glaser, P.H., 2011. Geophysical evidence for the lateral distribution of free phase gas at the peat basin scale in a large northern peatland. J. Geophys. Res. 116, G03008. http://dx.doi.org/10.1029/2010JG001543.

Pettinelli, E., Beaubien, S.E., Lombardi, S., Annan, A.P., 2008. GPR, TDR, and geochemistry measurements above an active gas vent to study near-surface gas-migration pathways. Geophysics 73, A11–A15. http://dx.doi.org/10.1190/1.2815991.

Plampin, M.R., Lassen, R.N., Sakaki, T., Porter, M.L., Pawar, R.J., Jensen, K.H., Illangasekare, T.H., 2014. Heterogeneity-enhanced gas phase formation in shallow aquifers during leakage of CO_2-saturated water from geologic sequestration sites. Water Resour. Res. 50, 9251–9266. http://dx.doi.org/10.1002/2014WR015715.

Poulsen, M.N., Kueper, B.H., 1992. A field experiment to study the behaviour of tetrachloroethylene in unsaturated porous-media. Environ. Sci. Technol. 26 (5), 889–895.

Roy, J.W., Ryan, M.C., 2010. In-well degassing issues for measurements of dissolved gases in groundwater. Groundwater 48, 869–877. http://dx.doi.org/10.1111/j.1745-6584.2010.00703.x.

Roy, N., Molson, J., Lemieux, J.-M., Van Stempvoort, D., Nowamooz, A., 2016. Three-dimensional numerical simulations of methane gas migration from decommissioned hydrocarbon production wells into shallow aquifers. Water Resour. Res. 52. http://dx.doi.org/10.1002/2016WR018686.

Royal Society, 2012. Shale Gas Extraction in the UK: A Review of Hydraulic Fracturing. Issued: June 2012 DES2597. The Royal Society and The Royal Academy of Engineering.

Schima, S., LaBrecque, D.J., Lundegard, P.D., 1996. Monitoring air sparging using resistivity tomography. Ground Water Monit. Remediat. 16, 131–138.

Sellwood, S.M., Healey, J.M., Birks, S., Butler Jr., J.J., 2005. Direct-push hydrostratigraphic profiling: coupling electrical logging and slug test. Groundwater 43 (1), 21–27.

Slater, L., 2007. Near surface electrical characterization of hydraulic conductivity: from petrophysical properties to aquifer geometries – a review. Surv. Geophys. 28, 169–197.

Slater, L., Comas, X., Ntarlagiannis, D., Moulik, M.R., 2007. Resistivity-based monitoring of biogenic gases in peat soils. Water Resour. Res. 43, W10430. http://dx.doi.org/10.1029/2007WR006090.

Strack, M., Mierau, T., 2010. Evaluating spatial variability of free-phase gas in peat using ground-penetrating radar and direct measurements. J. Geophys. Res. 115, G02010. http://dx.doi.org/10.1029/2009JG001045.

Sudicky, E.A., 1986. A natural gradient experiment on solute transport in a sand aquifer: spatial variability of hydraulic conductivity and its role in the dispersion process. Water Resour. Res. 22, 2069–2082.

Sudicky, E.A., Illman, W.A., 2011. Lessons learned from a suite of CFB Borden experiments. Groundwater 49, 630–648. http://dx.doi.org/10.1111/j.1745-6584.2011.00843.x.

Terry, N., Slater, L., Comas, X., Reeve, A.S., Schäfer, K.V.R., Zhongjie, Y., 2016. Free phase gas processes in a northern peatland inferred from autonomous field-scale resistivity imaging. Water Resour. Res. 52. http://dx.doi.org/10.1002/2015WR018111.

Thomson, D.A., 2004. Influence of Grain Size Variability and Sedimentology on Solvent DNAPL Distribution in the Borden Aquifer. MSc Thesis. University of Waterloo, Waterloo.

Thomson, N.R., Johnson, R.L., 2000. Air distribution during in situ air sparging: an overview of mathematical modeling. J. Hazard. Mater. 72, 265–282.

Tomlinson, D.W., Thomson, N.R., Johnson, R.L., Redman, J.D., 2003. Air distribution in the Borden aquifer during in situ air sparging. J. Contam. Hydrol. 67, 113–132. http://dx.doi.org/10.1016/S0169-7722(03)00070-6.

Trautz, R.C., Pugh, J.D., Varadharajan, C., Zheng, L., Bianchi, M., Nico, P.S., Spycher, N.F., Newell, D.L., Esposito, R.A., Wu, Y., Dafflon, B., Hubbard, S.S., Birkholzer, J.T., 2012. Effects of dissolved CO_2 on a shallow groundwater system: a controlled release field experiment. Environ. Sci. Technol. 47, 298–305.

Vidic, R.D., Brantley, S.L., Vandenbossche, J.M., Yoxtheimer, D., Abad, J.D., 2013. Impact of shale gas development on regional water quality. Science 340, 1235009. http://dx.doi.org/10.1126/science.1235009.

Wardlaw, N.C., 1982. The effect of geometry, wettability, viscosity, and interfacial tension on trapping in single pore-throat pairs. J. Can. Pet. Technol. 21, 21–27.

Yang, Q., Matter, J., Stute, M., Takahashi, T., O'Mullan, G., Umemoto, K., Clauson, K., Dueker, M.E., Zakharova, N., Goddard, J., Goldberg, D., 2014. Groundwater hydrogeochemistry in injection experiments simulating CO_2 leakage from geological storage reservoir. Int. J. Greenh. Gas Control 26, 193–203. http://dx.doi.org/10.1016/j.ijggc.2014.04.025.

Yang, X., Lassen, R.N., Jensen, K.H., Looms, M.C., 2015. Monitoring CO_2 migration in a shallow sand aquifer using 3D crosshole electrical resistivity tomography. Int. J. Greenh. Gas Control 42, 534–544. http://dx.doi.org/10.1016/j.ijggc.2015.09.005.